Hindawi
Advances in Materials Science and Engineering
Volume 2023, Article ID 9754687, 1 page
https://doi.org/10.1155/2023/9754687

Retraction

Retracted: Engineering Application of Nanomaterial and Ferroelectric Domain Polarization to the Dynamic Structure of the Surrounding Rock of Heavy-Duty Railway with Small Clear Intersection Tunnel

Advances in Materials Science and Engineering

Received 26 December 2023; Accepted 26 December 2023; Published 29 December 2023

This article has been retracted by Hindawi, as publisher, following an investigation undertaken by the publisher [1]. This investigation has uncovered evidence of systematic manipulation of the publication and peer-review process. We cannot, therefore, vouch for the reliability or integrity of this article.

Please note that this notice is intended solely to alert readers that the peer-review process of this article has been compromised.

Wiley and Hindawi regret that the usual quality checks did not identify these issues before publication and have since put additional measures in place to safeguard research integrity.

We wish to credit our Research Integrity and Research Publishing teams and anonymous and named external researchers and research integrity experts for contributing to this investigation.

The corresponding author, as the representative of all authors, has been given the opportunity to register their agreement or disagreement to this retraction. We have kept a record of any response received.

References

[1] X. Hao and H. Wang, "Engineering Application of Nanomaterial and Ferroelectric Domain Polarization to the Dynamic Structure of the Surrounding Rock of Heavy-Duty Railway with Small Clear Intersection Tunnel," *Advances in Materials Science and Engineering*, vol. 2023, Article ID 8354167, 13 pages, 2023.

Hindawi
Advances in Materials Science and Engineering
Volume 2023, Article ID 8354167, 13 pages
https://doi.org/10.1155/2023/8354167

Research Article

Engineering Application of Nanomaterial and Ferroelectric Domain Polarization to the Dynamic Structure of the Surrounding Rock of Heavy-Duty Railway with Small Clear Intersection Tunnel

Xiaotian Hao[1,2] **and Hailong Wang**[1,3]

[1]*School of Traffic and Transportation, Shi Jia Zhuang Tiedao University, ShiJiaZhuang 050043, HeBei, China*
[2]*School of Urban Construction Engineering, Chongqing Technology and Business Institute, ChongQing 400052, Chongqing, China*
[3]*School of Civil Engineering, Hebei University of Architecture, Zhangjiakou 075000, Hebei, China*

Correspondence should be addressed to Hailong Wang; bhxt196346@cqtbi.edu.cn

Received 5 September 2022; Revised 18 October 2022; Accepted 24 November 2022; Published 7 February 2023

Academic Editor: Haichang Zhang

With the development of national railways and railways as one of the important channels for heavy-haul transportation, the construction of heavy-haul railways must be a rapid development, which makes it inevitable that the heavy-duty situation of small-distance interchange tunnels will appear. Nanomaterials refer to materials that have at least one dimension in the three-dimensional space in the nanoscale range (1 nm~100 nm) or are composed of them as basic units. Ferroelectric domain polarization refers to the existence of electric domains in ferroelectrics, electric domains refer to small regions with the same spontaneous polarization direction, and the boundaries between electric domains and electric domains are called domain walls. It is also urgent to study the dynamic structure of the surrounding rocks of heavy-duty railways. This article aims to study the use of nanomaterial and ferroelectric domain technology to improve the overall strength, wear resistance, toughness, and other properties of steel to ensure the safety of the surrounding rock dynamic structure of the heavy-duty railway in the small clearance intersecting tunnel. Moreover, on this basis, this article proposes the method of spraying steel with nanomaterials and the use of ferroelectric domain polarization technology. The strength and wear resistance of steel can be improved under different nanomaterial content and the degree of ferroelectric domain polarization. Sustainability and toughness have been improved, respectively. After the wear resistance experiment and analysis, the experimental results of this article show that the impact resistance of the steel increased by 18.75%. When 0.012% of CeO_2 is added, the impact toughness of the steel is increased to the maximum of 3.4 J, an increase of 16.31%, and a 37% increase in wear resistance. Under the premise of ensuring the demand for heavy-duty transportation, the safety performance and sustainability of transportation are greatly improved.

1. Introduction

As an important national transportation carrier, railways provide a good guarantee of transportation capacity for the progress and development of society. From its initial development to the present stage, the railway has always been in a dominant position among the five major modes of transportation. Based on the advantages of low energy consumption, large transportation capacity, low environmental pollution, and safe and reliable transportation process, it undertakes most of the long- and short-distance passenger and cargo transportation. In recent years, with the development of new technologies and the development of high-tech train types, its status as the backbone of land transportation has become prominent. Countries in the world gradually regard railways as their main development direction in both passenger and freight transportation. With the development of the economy, people pay more and more

attention to the requirements of high speed, large transportation volume, and low investment. The construction and development of heavy haul railways are gradually put on the agenda of various countries.

Heavy-duty rail transportation first started in the United States. Under the demand for the transportation of ore, raw materials, and coal, they have begun to vigorously develop heavy-haul railways. The development of heavy-haul railways is mainly reflected in the increase in line traffic and train axle loads. Domestic research on heavy-haul railways began in the 1980s. In recent years, research on heavy-haul railways has achieved considerable results. Based on the two development directions of heavy-haul railways, two modes of development of heavy-haul trains on the main heavy-haul lines such as Daqin and Shuohuang Coal Special Lines and Beijing-Guangzhou and Beijing-Shanghai have mainly formed. With the increasing maturity of heavy-duty technology, Daqin Line successfully trial-run 30,000-ton trains in April 2014, which is also a sign that domestic heavy-duty technology has entered the international ranks. Therefore, the development of heavy-haul railways still requires innovation in key technologies and countermeasures.

With the development of science and technology, the technology of railway manufacturing has been gradually improved, which has been a hotly discussed issue by scholars from all walks of life in recent years. The requirements for heavy loads on cargo and manned railways are also getting higher and higher. As one of the first choices for transportation, railways are The improvement and construction of the railway are also urgent, and the rapid development of nanomaterials and ferroelectric domain polarization is that some people have proposed to apply them to the dynamic structure of the heavy-duty railway surrounding rock of the country's small-distancethree-dimensional tunnels to enhance the heavy-duty of the railway. In his article, Rzayev emphasized the ability of the molecular bottle brush as a highly adjustable building block for the creation of nanostructured materials through molecular templates, solution aggregation, and melt self-assembly. Future opportunities in the field of polymer science are briefly discussed, and the most recent developments in the synthesis of discrete nano-objects, micellar structures, and periodic nanomaterials from brush copolymers are highlighted. Solution polymerization is a crucial synthetic technique in the production of polymers. In most cases, it is carried out at the solvent's reflux temperature, which effectively regulates the reaction temperature and allows the solvent to evaporate, dissipating the heat produced by the exothermic reaction [1]. The research on nanostructured materials is far more than that. For example, Wiemann et al. believe that most of the in vitro studies investigating the pulmonary toxicity of nanomaterial have a poor correlation with in vivo inhalation studies. Alveolar macrophages (AMs) play a prominent role during inhalation exposure because they effectively clear the alveoli from the particles. This study addresses the applicability of the in vitro alveolar macrophage assay in distinguishing between bioactive nanomaterials and passive nanomaterials, lung macrophages are differentiated from monocytes and are widely distributed in the pulmonary interstitium, with more around the ducts below the bronchioles and in the alveolar septa [2]. This article explores the application of nanomaterials in cytology. Not only that but also the application of nanomaterials in other areas. Lithoxoos et al. use Grand Canonical Monte Carlo (GCMC) simulations combined with ab initio QM calculations to study the adsorption capacity of H_2 in single-walled silicon nanotubes (SWSiNT) assuming an armchair structure model. The interaction between H_2 and the graphite-like sheet on a single SiNT surface calculated from QM can be fitted to an accurate potential function for the simulation system. This theoretical method is also used for SWCNTs with similar properties and the same thermodynamic state. The GCMC simulation of the NT beam and H_2 shows that compared with CNT, the adsorption of SiNT to H_2 is enhanced [3]. We can have a good understanding of nanomaterials by appealing to the research reference of nanomaterials. The research on ferroelectric domain polarization can be understood through the following article. Yamaguchi et al. theoretically revealed that weak light excitation achieves about 18% of the electrode polarization inversion, which is interpreted as the superposition of multiple excitonic states. The charge-ordered ferroelectric ground state from (TMTTF) (2) PF6 is in absolute zero temperature. Therefore, a Delta P/P value similar to 36% can be expressed as being achieved in the early stages of the material's ultrafast photodynamics. This fact applies not only to the application of this material and other similar materials in optical devices but also to the study of electrical polarization controlled by light, which is one of the most attractive issues in the phenomenon of photoinduced phase transition [4]. However, the author only conducted relevant research on it theoretically and did not rely on a large number of practical operations, so the reliability of the article was not high. Shin and Son believe that polycrystalline $YMnO_3$ (YMO) films are deposited on (111) Pt/Ta/glass substrates by pulsed laser deposition (PLD). Due to the high crystallinity produced, the low PLD deposition rate can reduce the leakage current of YMO films. The YMO film exhibits a strong ferroelectric response, including a residual polarization of 4.2 μC/cm. Piezoelectric response force microscopy studies have shown that the YMO film has a mosaic domain structure, and the ferroelectric domain wall energy is lower than that of the $PbTiO_3$ film [5]. However, the fast switching speed of the capacitor in the article is too slow. It is recommended that the fast switching speed of YMO capacitors lower than 85 ns can be more effectively derived from this low domain wall energy. In his work, Gonçalves et al. studied the ferroelectric domain structure of (Pb.La.)TiO transparent ceramics and its response to an external electric field through piezoelectric response force microscopy (PFM) [6]. By responding to the ferroelectric domain structure and its applied electric field, we can have a better understanding of its field. The relevant research on heavy-load railways is as follows: Yan et al. deal with several types of angled rail defects by simulating the acceleration system installed on the locomotive and theoretically studying the feasibility of monitoring angled rail joint defects. The quantitative relationship between the axle box acceleration characteristics (peak-to-peak value) and rail defects was determined by simulation [7]. This research is of great significance for the daily maintenance of heavy-haul railways. Cai

et al. comprehensively studied the dynamic characteristics of a new type of track that uses polyurethane foam to cure ballast in heavy-duty railway tunnels. Based on the multibody system dynamics theory and finite element method, a dynamic model of the vehicle-track-tunnel interaction system is established, the dynamic influence of the polyurethane foam-cured ballast track on the train, and surrounding infrastructure is calculated. The results show that the polyurethane foam curing ballast reduces the track stiffness and vibration acceleration of the tunnel without affecting the vehicle derailment coefficient and wheel load reduction rate [8]. The previously mentioned articles have carried out relevant research on nanomaterials, heavy-duty railways, and ferroelectric domain polarization, but the conclusions of the research are still not perfect, and the research effect of the content of this article is not great.

Due to the tremendous load of the railway, the surrounding rock structure of the heavy-duty railway built on the original limited clearance crossing tunnel is vulnerable to deterioration, as well as the impact on the tunnel's structure, resulting in a decrease in the safety of the tunnel structure, but the heavy-duty railway is also a country It is one of the indispensable transportation methods in the development stage, so this article takes into account this situation, and for the first time innovates the method of nanosprayed steel and ferroelectric domain polarization to strengthen the surrounding rock structure and the overall structure of the tunnel. The safety strengthens its strength and wear resistance so that while the carrying capacity of heavy-duty railways can be guaranteed, safety is also guaranteed. The innovation of this paper is the analysis of the railway tunnel structure based on nanotechnology and ferroelectric domain polarization.

2. Spraying Nanomaterials and Ferroelectric Domain Method

2.1. Nanomaterial Preparation Method. Nanomaterials have gradually become a major application-oriented new material to improve the characteristics of traditional materials with their unique mechanism and performance. Nanomaterials are used more and more in engineering. For example, copper nanoparticles are used to reduce the surface roughness of steel to facilitate welding and prevent surface corrosion; nanomaterials are used in Roman churches as catalysts to improve their own cleanliness function; adding nanosilica particles to fill the pores in the concrete, reducing the segregation in the concrete self-compacting process, making it stronger, more durable, and more sustainable; using nanosensing to detect the health of the concrete during construction [9].

The chemical method is the most commonly used method for preparing nanomaterials, which can be roughly divided into the hydrothermal method and the hydrolysis method. The chemical method refers to the use of reversible chemical reactions to convert compounds with specific functional groups in natural essential oils into intermediate products that are easy to separate. After separation and purification, the intermediate products are restored to the original spices. This method is called chemical treatment. In particular, nano-oxide particles generally adopt the hydrothermal method. In addition, the nanomaterial preparation process can also adopt a complex process combination method, such as a composite process of the physical vapor method and the chemical deposition method. In this paper, the preparation process of nanomaterials is shown in Figure 1.

Nanomaterials only refer to the types of materials with a certain particle size level, and the real nanomaterials used in engineering are limited. There are three main types of nanomaterials commonly used in engineering, carbon nanotubes, nanosilica, and Mibetoni, as shown in Figure 2:

2.1.1. Carbon Nanotubes. Carbon nanotubes have superplasticity and Poisson's ratio and are often used to strengthen the strength of metals. At the same time, carbon nanotubes can be used as cement additives to enhance the compactness of cement.

2.1.2. Nanosilica. The shear strength of the soil after nanosilica treatment is greatly enhanced, and it can effectively prevent soil liquefaction.

2.1.3. Nanobetonies. Bentonite is mainly composed of montmorillonite, nanobentonite roommate volcanic ash weathered clay minerals; nanobentonite has higher purity than natural bentonite [10].

2.2. Phase Field Simulation and Finite Element Method. With the rapid development of computer technology, computer simulation technology, material thermodynamics, dynamics, etc. have been improved to a considerable extent, and the phase field model has been developed rapidly, and it has become a more effective method of material simulation. Finite element analysis is used to transform difficult issues into more manageable ones before solving them. It seems the problem domain as being composed of a number of tiny, interconnected subdomains known as finite elements, assumes an acceptable approximation for each element, and then derives the overall satisfactory criteria for solving this domain in order to arrive at the solution to the problem.

In the influence on the ferroelectric domain structure and its polarization this time, we use this method to study it and briefly explain its basic idea.

2.2.1. Introduction to Classic Phase Field. The theoretical basis of the phase field method is the Ginzburg–Landau theory. The Ginzburg–Landau theory (GL Theory) is an important phenomenological superconductivity theory (1950). Compared with the London equation and Pippard's nonlocal theory, the unique feature of GL theory is that it can deal with the situation of a strong magnetic field and superconducting electron density in space. The origin of the phase field method is deeply influenced by the average field theory of the first and second phase transitions. In the beginning, it used the average field theory to discuss a series

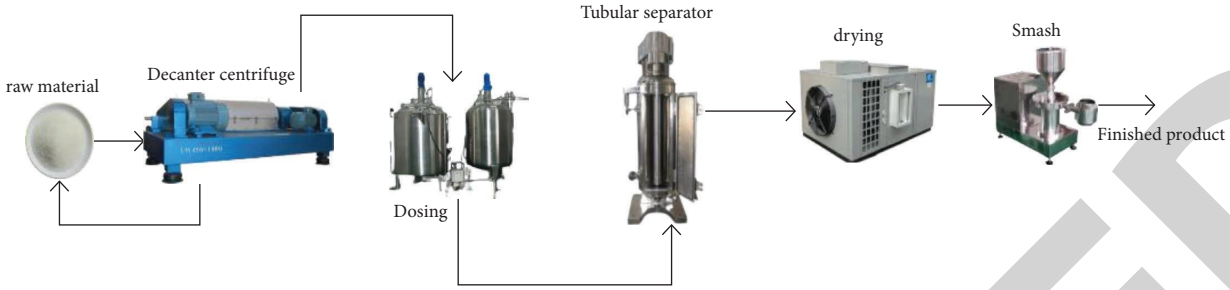

Figure 1: Physical picture of the preparation process of nanomaterials.

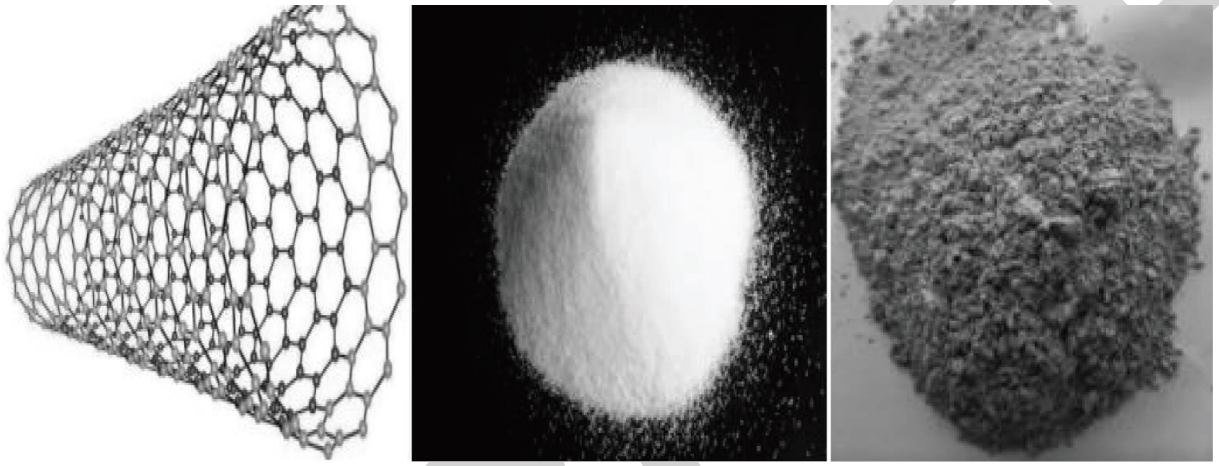

Figure 2: Three common nanomaterial's in engineering.

of simple phase transitions. Based on this, different evolution equations are selected according to the types of order parameters.

The phase field method is used to study ferroelectric thin film materials, which takes polarization as the order parameter and uses the principle of minimum energy to simulate the evolution of domain structure under the action of the driving force. Therefore, the evolution equation we use is as follows:

$$\frac{\partial P_i(s,t)}{\partial t} = -L\frac{\delta F}{\delta P_i(s,t)}, \quad (i = 1,2,3), \tag{1}$$

$$F = \int_V f dV. \tag{2}$$

Equations (1) and (2) use t to represent time and s to represent a vector in space. P represents the polarization value at a certain time and position and L represents the corresponding dynamic coefficient, which can be regarded as a generalized electric field, which represents the thermodynamic driving force [11]. The general expression of Landau–Devonshire free energy density is as follows:

$$f = f_{\text{landau}} + f_{\text{strain}} + f_{\text{coup}} + f_{\text{grad}} + f_{\text{elec}}. \tag{3}$$

Among them, f is expressed as density. The model is established as follows: Three physical fields—polarization field, electric field, and displacement field—are necessary to model the coupling behavior of pseudoferroelectric materials under electric and force fields. Therefore, the basic physical quantities used to describe the thermodynamic state are displacement (u), stress (σ), strain (ε), electric potential (ϕ), electric field (E), electric displacement (D), polarization (P), and polarization Gradient (∇P). The first Landau free energy density can be written as follows:

$$f_{\text{landau}} = \frac{1}{2}a_{xy}p_x p_y + \frac{1}{4}\beta_{xyzq}p_x p_y p_z p_q + \frac{1}{6}\gamma_{xyzqwe}p_x p_y p_z p_q p_w p_e. \tag{4}$$

The presence of spontaneous polarization or substrate strain binding in the ferroelectric thin film will cause the lattice to strain, so the elastic strain energy density of the system can be expressed as follows:

$$f_{\text{strain}} = \frac{1}{2}w_{11}\left(\varepsilon_{11}^2 + \varepsilon_{22}^2 + \varepsilon_{33}^2\right) + w_{12}\left(\varepsilon_{11}\varepsilon_{12} + \varepsilon_{22}\varepsilon_{33} + \varepsilon_{11}\varepsilon_{33}\right) + 2w_{44}\left(\varepsilon_{12}^2 + \varepsilon_{23}^2 + \varepsilon_{13}^2\right), \tag{5}$$

where w represents the flexibility coefficient of shorthand notation and ε represents the strain of the system. We use O to represent the electrostriction coefficient in shorthand notation.

$$f_{\text{coup}} = -O_{11}\left(\varepsilon_{11}p_1^2 + \varepsilon_{22}p_2^2 + \varepsilon_{33}p_3^2\right) - O_{12}\left[\varepsilon_{11}\left(p_2^2 + p_3^2\right) + \varepsilon_{22}\left(p_1^2 + p_3^2\right) + \varepsilon_{33}\left(p_1^2 + p_2^2\right)\right]. \tag{6}$$

Polarization gradient energy density is also called domain wall energy density.

$$f_{\text{grad}} = \frac{1}{2}T_{11}\left(p_{1,1}^2 + p_{2,2}^2 + p_{3,3}^2\right) + T_{12}\left(p_{1,1}p_{2,2} + p_{2,2}p_{3,3} + p_{1,1}p_{3,3}\right). \tag{7}$$

Among them, we use T to represent the gradient coefficient and p to represent the polarization gradient [12].

The electrostatic energy density is determined by the depolarization field and the applied electric field.

$$f_{\text{elec}} = -\frac{1}{2}\varepsilon_0\varepsilon\left[(E_1)^2 + (E_2)^2 + (E_3)^3\right] - (E_1p_1 + E_2p_2 + E_3p_3). \tag{8}$$

2.2.2. Among Them, The Constitutive Equation for Each Field can be Derived from the Free Energy Density.

$$\sigma_{xy} = \frac{\partial h}{\partial \varepsilon_{xy}} = c_{xymn}\varepsilon_{we} - \frac{1}{2}q_{xymn}p_wp_e, \tag{9}$$

$$D_x = -\frac{\partial h}{\partial E_x} = -k_0E_x - p_x, \tag{10}$$

$$\eta_x = \frac{\partial h}{\partial p_x} = \alpha_{xy}p_y + \beta_{xymn}p_yp_mp_n + \gamma_{xymnwe}p_yp_mp_np_wp_e - O_{mnwe}\varepsilon_{mn}p_y - E_x, \tag{11}$$

$$\Lambda_{xy} = \frac{\partial h}{\partial p_{x,y}} = g_{xymn}p_{m,n}. \tag{12}$$

From equations (9)–(12), it is not difficult to see that the three fields of the displacement field, polarization field, and electric field are completely coupled.

2.2.3. Balance Conditions of Each Field. The three balance equations are as follows:

The balance equation that force satisfies is

$$\left(\sigma'_{xy} - t'_{xym,n}\right) + b_k = 0. \tag{13}$$

The control equation for polarization is as follows:

$$\frac{\partial P_x}{\partial t} = -L\left[\eta'_{xy} - \Lambda'_{xy,y}\right]. \tag{14}$$

The governing equation of the electric field is Maxwell's equation.

$$D'_{x,y} - \zeta = 0. \tag{15}$$

Here, we assume that the volume of the material under study is V and the surface area is S, so we can get the following:

$$\begin{aligned} u_x &= \overline{u_x} \quad \text{on } S_u \\ n_x\sigma_{xy} &= T_y \quad \text{on } S_\sigma. \end{aligned} \tag{16}$$

The T in the formula is expressed as the face force component. It should be noted that force and displacement cannot be given at the same point at the same time, but at each boundary point, one of them must be given. This is expressed as follows:

$$\begin{aligned} S_u \cap S_\sigma &= 0, \\ S_u \cup S_\sigma &= S. \end{aligned} \tag{17}$$

The boundary conditions of electric potential or surface charge density are as follows:

$$\begin{aligned} Z &= \overline{Z} \quad \text{on } S_Z, \\ n_xD_x &= -w \quad \text{on } S_w, \\ S_Z \cap S_w &= 0, \\ S_Z \cup S_w &= S. \end{aligned} \tag{18}$$

The boundary condition of the polarization field is polarization P or surface polarization gradient flux.

$$\begin{aligned} n_x\Lambda_{xy} &= \frac{\partial h}{\partial P_{x,y}}, \\ n &= \pi_y \quad \text{on } S_\pi. \end{aligned} \tag{19}$$

In the above formula, S is used to represent the polarization gradient flux boundary.

2.3. Methods of Small Clearance Interchange Tunnels. This paper combines the small-distance tunnel project between Sungang Station and Honghu Station of Shenzhen Metro Line 7, and comprehensively adopts research methods such as technical investigation, theoretical analysis and numerical simulation, model test, and induction and summary. The influence of the change of the tunnel clear distance has been studied in depth [13]. The main technical roadmap is shown in Figure 3:

In order to ensure that the model test results can reflect the real situation, the test model is required to be able to simulate the stratum and the tunnel in terms of shape and material physical and mechanical properties. In order for the model to produce physical and mechanical phenomena similar to the prototype in the test process, it is required that

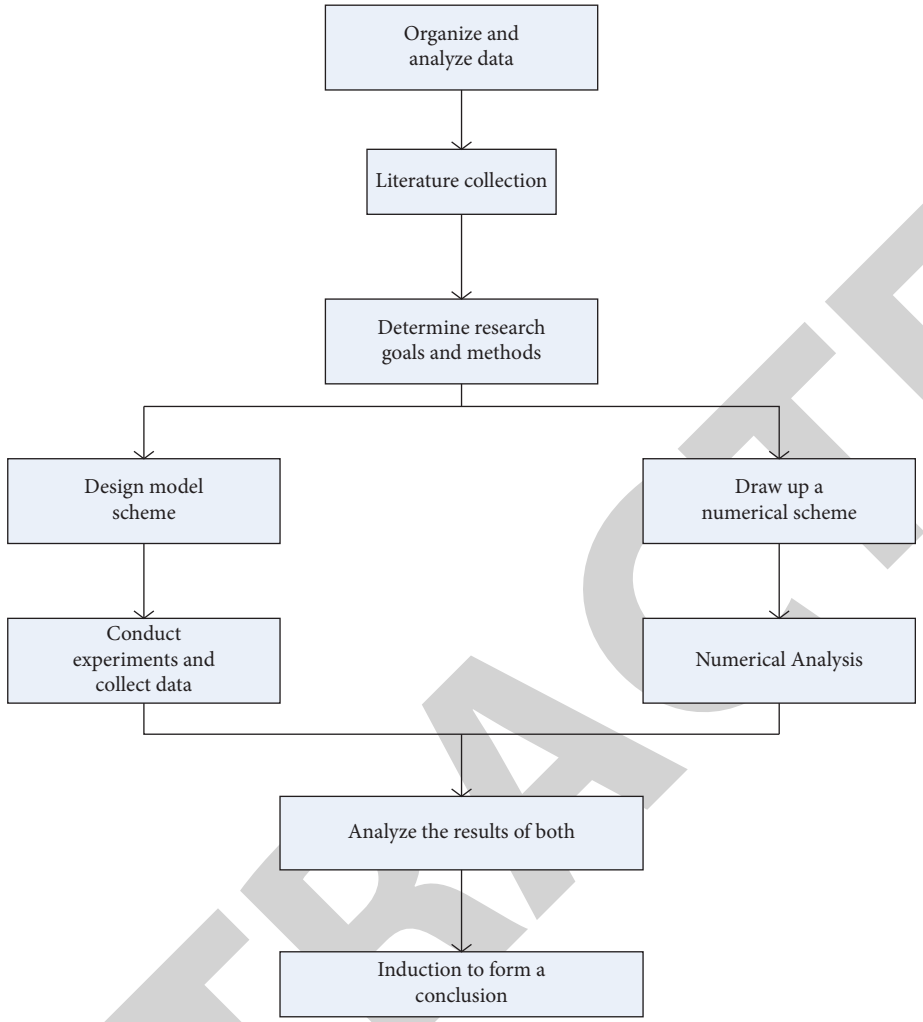

Figure 3: Main technical roadmap.

the material, shape, and load of the model have certain similarities with the prototype [14].

3. Railway Heavy Load Damage Test

3.1. Features of Heavy-Duty Railway Tunnels. The operating characteristics of domestic heavy-duty railway tunnels mainly include the following three points:

Feature 1: the shaft is heavy and the total weight is shown in Table 1. Table 1 shows the comparison of the axle load and total weight of domestic heavy-duty railway trains, high-speed railways, and subways.

It can be seen from Table 1 that the axle load of heavy-duty trains increased by 75% compared with that of subways, and that of higher trains increased by 40%. The total weight is 13 times that of the subway and 6 times that of the high-speed rail. The axle load of the subway is 15 tons, the axle load of the high-speed rail is 19 tons, and the axle loads of the two trains are 650 and 1,300 tons, respectively. Therefore, the large axle load and the large total weight will inevitably cause the structure of the tunnel bottom to bear the greater load, thereby intensifying the fatigue damage of the tunnel surrounding rock and inverted structure.

Feature 2: high driving density. Table 2 shows the comparison of traffic density and frequency of domestic heavy-haul railways, high-speed railways, and subways.

It can be seen from Table 2 that the frequency of a single heavy-duty train on the tunnel structure is 11 times that of the subway and 7 times that of the high-speed rail; the frequency is about 12 times that of the subway and 7 times that of the high-speed rail. In addition, compared to the 4 hours of skylight time of subway and high-speed rail, the skylight time of heavy haul railway is only 2 hours. Therefore, the heavy-duty railway tunnel bottom structure bears a long time for one action and a longer total action time, which requires higher structural durability, but the available maintenance time is short. This leads to the need for materials used in the manufacture of railways. Even more, consideration is given to durability [15].

Feature 3: the main transport is coal. At present, domestic heavy-haul railways are mainly used for coal transportation, and the cinder produced during coal transportation has a non-negligible impact on the central drainage ditch and internal environment of the heavy-haul railway tunnel, as shown in Figure 4.

Table 1: Comparison of various train parameters.

Train type	Gross weight (t)	Train axle load (t)
Subway	15	650
High-speed rail	19	1300
Heavy-duty train	75% more than the subway 40% more than high-speed rail	13 times the subway 6 times of high-speed rail

Table 2: Comparison of various train lengths and their frequency of use.

Train type	Number of cars	Length	Frequency of use
Subway	8	244	42
High-speed rail	15	400	60
Heavy-duty train	11 times the subway 7 times the subway	6 times the subway 4 times the subway	12 times the subway 7 times the subway

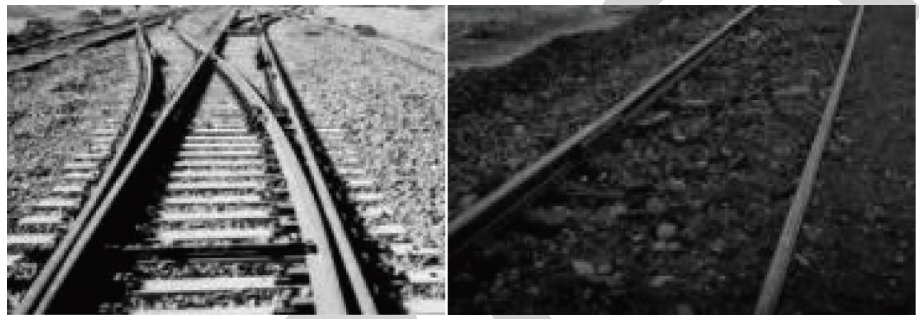

Figure 4: Comparison of ordinary railways and heavy-duty coal railways.

According to the areas of occurrence, we also divided the structural diseases of heavy-duty railway tunnels into the following two major categories: structural diseases of the upper arch wall and structural diseases of the lower tunnel floor. The specific types are shown in Table 3.

From Table 3, it can be seen that the core samples obtained in some sections have traces of cavities, damages, and fractures. The test results are systematically analyzed and it is found that the measured thickness of the base concrete of the diseased section of the line basically does not meet the design requirements and the bottom structure of some tunnels. The damage to concrete is the most common, and it is manifested as the worse the grade of the surrounding rock, the more serious the disease at the bottom of the tunnel [16].

3.2. Model Experiment of the Impact of the Clear Distance of the Tunnel with Small Clear Distance. Based on the actual engineering situation and combined with the corresponding conditions of the model test, the geometric similarity ratio of this model test is finally determined to be 35 : 1. The similarity ratio of each parameter in the test can be easily obtained by Buckingham's theorem, as shown in Table 4.

In Table 4, the geometric similarity ratio reaches 35%, the bulk density similarity ratio is 1%, and the strain similarity ratio and the internal friction angle similarity ratio are 1%.

Table 3: Types of diseases in heavy-duty railway tunnels.

Injury site	Type
Upper arch wall structure	Water leakage Cracking Corroded off blocks Structural deformation
Lower tunnel bottom structure	Foundation bed sinks Mud and mud Squeeze Damage to the paving structure

3.3. Experimental Materials

3.3.1. Surrounding Rock Materials. The test surrounding rock grades is planned to be IV and V grades. The related physical and mechanical performance indexes of surrounding rock materials used in the test are shown in Table 5.

3.3.2. Lining Materials. This test is mainly to study the regularity of the influence of the excavation of a new shield tunnel on the existing tunnel. The lining section of the model test is a circular section [17]. Relying on the project, the outer diameter of the subway shield tunnel is 6 m, the lining thickness is 0.3 m, the buried depth of the right-line tunnel is 6 m~17 m, and the buried depth of the left-line tunnel is 14~26 m, as shown in Figure 5.

Table 4: The similarity ratio of each parameter of the model experiment.

Name	Proportion
Geometric similarity ratio	35
Cohesion similarity ratio	35
Displacement similarity ratio	35
Bulk density similarity ratio	1
Stress similarity ratio	35
Elastic modulus similarity ratio	35
Strain similarity ratio	1
Internal friction angle similarity ratio	1

Table 5: Physical and mechanical performance parameters of surrounding rock materials in model tests.

Level	Elastic modulus	Capacity	Cohesion	Poisson's ratio	Friction angle
IV	14	15	0.8	0.28	30
V	18	17.5	1.2	0.39	45

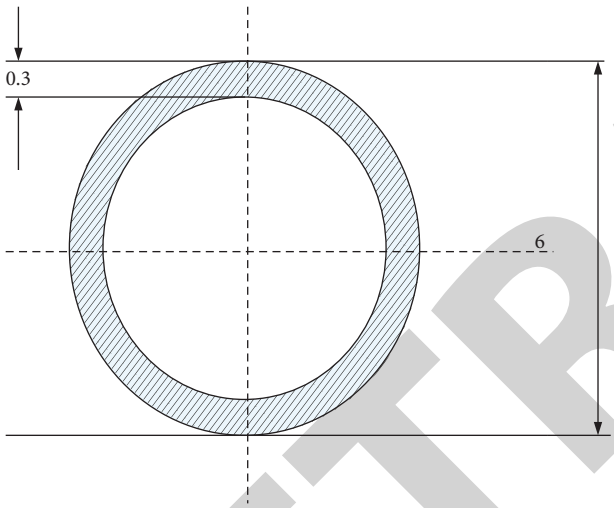

Figure 5: Sectional view of the lining structure of a shield tunnel.

According to the geometric similarity ratio, the lining structure size of the model can be calculated to be 200 mm in diameter and 10 mm in thickness. Therefore, in the actual experiment, a PVC pipe with a diameter of 200 mm and a thickness of 4 mm is used. In order to ensure the physical and mechanical properties of the lining material in the model test [18].

3.3.3. Test Procedure

(i) Place the planks and fill them with soil to the height of the bottom of the left tunnel model

(ii) Place the model of the left line of the tunnel, and continue to fill up to the height of the bottom of the right line of the tunnel

(iii) Fill the tunnel to the right and place it at the design height

(iv) Fill up the soil in the upper part of the tunnel layer by layer

(v) Place the displacement gauge in the left lane tunnel

(vi) Let it solidify for 24 hours

(vii) Connect the test system, record the initial value, and reset the displacement meter

(viii) Simulate the excavation of the right-line tunnel, and record various data after stabilization

Corresponding strains arranged along the ring from the inside and outside of the lining can be measured according to the corresponding strain data recorded by the strain tester. The tunnel structure is located in the surrounding rock. The new tunnel is constructed close to the existing tunnel, and the impact of the two tunnels is complicated. Through the numerical calculation method, the influence of the new tunnel excavation on the existing tunnel when the two tunnels are overlapped and parallel under different clearance conditions is analyzed. It analyzes and summarizes the ground settlement, the displacement of the existing tunnel lining, the bending moment and the axial force change value, and the distribution of the plastic zone, and systematically analyzes the close construction of the small clear distance tunnel, especially when the clear distance is less than 1 times the diameter of the new tunnel. The influence law of the existing tunnel [19].

3.4. Ferroelectric Domain Wall Structure Experiment. This experiment mainly conducts detailed theoretical analysis and experiments on domain structure, analyzes the correlation between domain growth, polarization, and stress, and measures the domain stress on the X plane and the energy density of the domain wall according to their interface and at the same time derives The domain wall energy of the Y plane [20].

It is generally believed that the width of the domain wall is only on the order of a few unit cells, which means that only a few unit cells are required to deform the positive and negative domain structure. However, the stress and optical birefringence caused by domain walls can extend to the order of micrometers.

The experimental equipment is mainly composed of a liquid electrode filled with tap water. The liquid electrode

allows us to observe the domain wall with a polarizing microscope while using an external electric field to control the movement of the domain wall. A 532 nm laser is used to irradiate the crystal to generate photo-generated carriers. The carriers move under the lateral shielding field generated by the domain wall to form domain wall imprints [21]. All experimental images are recorded by the CCD connected to the microscope. The process of generating and erasing domain wall imprints is shown in Figure 6.

We found that the 600 nm laser with the same light intensity and the same irradiation time could not produce and eliminate domain wall imprints, while the use of a mercury lamp with a center wavelength of 345 nm could eliminate but not produce imprints. We believe that the formation of domain wall imprinting is due to the migration of electrons inside the crystal under the action of the horizontal shielding field on the surface.

An important question is where these photo-generated electrons come from. All visible light and ultraviolet light cannot excite electrons from the forbidden band to the conduction band. However, there are some electrons in defective energy levels that can be excited by specific light. Taking into account that the samples we use are all photorefractive materials, red light cannot produce and erase the mark; we believe that the electron comes from a bipolaron. In the case of ultraviolet light irradiation, electrons can still be excited, but they have greater energy and thus break away from the surface dielectric layer and become free electrons in the liquid electrode. Their movement greatly weakens the horizontal shielding electric field. Therefore, although more electrons are excited by the purple light, the purple light also makes the charge distribution at the original domain wall of the crystal tend to be uniform, so there is no domain wall imprinting. Long-term green or violet light irradiation can re-excite the electrons in the crystal. Since the photoconductance of the crystal is much larger than the dark conductance, the electron movement speed is accelerated, and the charge density distribution quickly tends to balance, so the imprint is also eliminated [22]. To sum up, the research on the problem of heavy haul railway structure and the proposed countermeasures have laid the foundation for economic development.

4. Intersection Tunnels with Small Clear Distance

4.1. Dynamic Response Analysis of the Upper-Span Tunnel. Under the load of the upward train, the displacement time-history curve of each observation point of the conventional section of the upper-span tunnel and the upper-span tunnel interchange section is shown in Figure 7.

It can be seen from Figure 7 that the closer the structural parts of the lining are to the train load, the greater the maximum vertical vibration displacement. Among them, the displacement response of the track bed and the arch bottom is the largest, and the vault top is the smallest. The maximum vertical displacement of the track bed of the overpass tunnel is increased by 60.4% compared with the track bed of the conventional section [22]. In addition, the displacement of each observation point of the overpass section of the upper-span tunnel is greater than that of the conventional section, indicating that the overpass section is a dangerous section during train operation.

The acceleration time-history curve of each observation point of the conventional section of the upper-span tunnel and the upper-span tunnel interchange section is shown in Figure 8.

From Figure 8, it can be seen that under the load of the upward train, the acceleration time history curve law of each observation point is basically the same, and all exhibit vibration characteristics. Since the ascending train load passes through the conventional section of the upper-span tunnel first and then passes through the overpass section, the acceleration of the conventional section shows a clear vibration trend at the start of the train operation, while the acceleration of the overpass section vibrates around 0 at the beginning. In addition, the acceleration peak of the interchange section also lags slightly behind the conventional section. When the train passes through each section completely, the acceleration eventually approaches zero [23].

4.2. Dynamic Response of Underpass Tunnel. The regular section of the underpass tunnel and the underpass section of the tunnel are basically the same in the displacement time history curve of each observation point, the numerical value is different, and both show the characteristics of vibration. Since the load of the upward train is far from the conventional section of the tunnel underneath, when the train runs for a certain period of time, the vertical displacement begins to vibrate. When the upward train runs, the vertical displacement of each section of the tunnel underneath all tends to vibrate near zero. The displacements of the observation points of the conventional section of the underpass tunnel are almost equal and small, indicating that the upward train load has almost no effect on the conventional section of the underpass tunnel. The maximum vertical displacement of each part of the underpass tunnel cross-section is greater than that of the conventional underpass tunnel [24]. In addition, the closer the structural parts of the lining are to the train load, the greater the maximum vertical vibration displacement. It indicates that the arch top of the underpass tunnel cross-section is a dangerous part, and the cross-section is a dangerous section. The maximum vertical vibration displacement of the cross-section of the underpass tunnel is, in descending order, arch top, arch shoulder, sidewall, arch foot, track bed, and arch bottom. The vertical displacement changes and acceleration peak trends of each observation point are shown in Figure 9.

It can be seen from Figure 9 that the acceleration of each part of the tunnel lining structure underneath gradually decreases as the distance from the train load increases. Among them, the peak acceleration at the dome is the largest. Since the conventional section of the underpass tunnel is far away from the ascending train load, the acceleration peaks of all observation points are small, among which the acceleration of the vault is larger. As can be seen from the figure, the speed of the shift is slower than that of

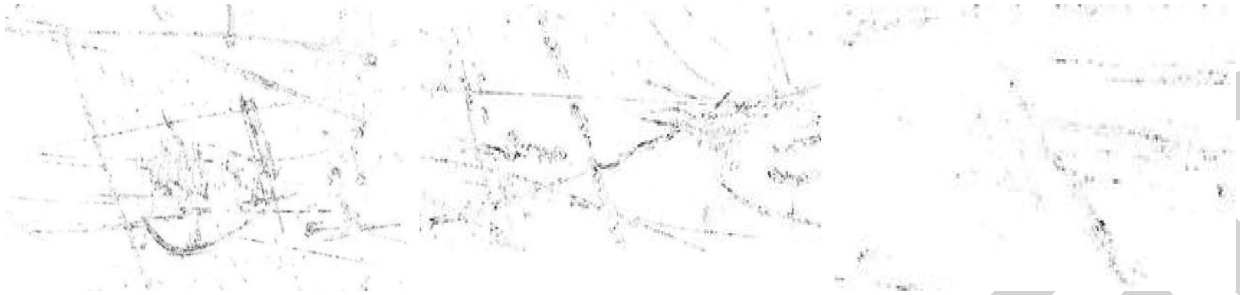

Figure 6: Generation and erasure process of domain wall imprints.

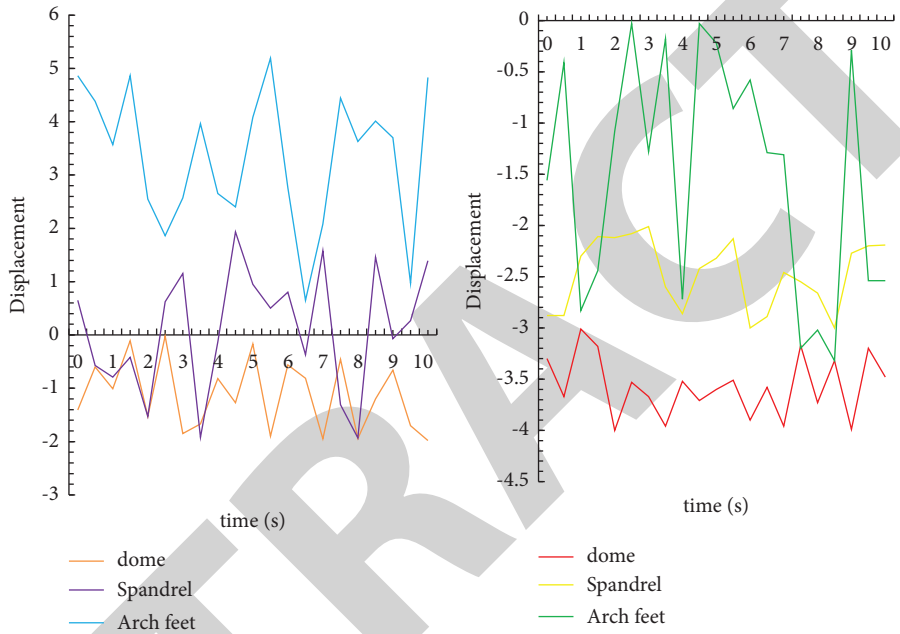

Figure 7: Displacement time-history curve of each observation point of the conventional and interchange sections of the upper-span tunnel.

the acceleration, and it is roughly full around 40. It can be seen that the upward load has almost no effect on the acceleration response of the conventional section of the underpass tunnel. Because the cross-section of the underpass tunnel is closer to the upward load, the acceleration peaks at each observation point are larger than the conventional cross-section of the underpass tunnel. Among them, the acceleration peak value at the vault position of the underpass tunnel cross section is the largest [25].

4.3. Impact Analysis of Clear Distance When Two Tunnels Overlap. This section mainly analyzes the influence of the right (upper) tunnel excavation on the left (lower) tunnel when the two tunnels overlap, that is, when the angle of the two tunnels is 90°, including lining displacement, segment bending moment change value, axial force change value, the law of influence, as shown in Figure 10.

It can be seen from Figure 10 that when the two tunnels overlap, as the clear distance between the two tunnels increases, the impact of the right tunnel excavation on the displacement change value of the left tunnel generally shows a weakening trend. The clear distance between the two tunnels increases, the vault displacement change value decreases, and the right arch waist displacement change decreases. When the two tunnels overlap, the impact of the right (upper) tunnel excavation on the left (lower) tunnel vault is obviously stronger than the arch bottom, and the impact on the arch waists on both sides is basically the same. Comparing the test results under the condition of the same clear distance, when the two tunnels overlap, the impact on the left line (existing) tunnel lining is more significant than when the two tunnels are parallel to the right line (newly built) tunnel. When the tunnel is located above the left (existing) tunnel, its excavation unloading effect is more significant than when the two tunnels are parallel.

4.4. Wear Test and Friction Coefficient Analysis. Through subsections 2.1 and 2.2 of this article, it can be seen that the wear performance of steel with different contents of nanomaterials is very excellent. Therefore, in this wear resistance experiment and friction coefficient analysis, in the wear test of steel with different contents of nano-CeO_2, a larger load is selected (20 N) to further discuss the research

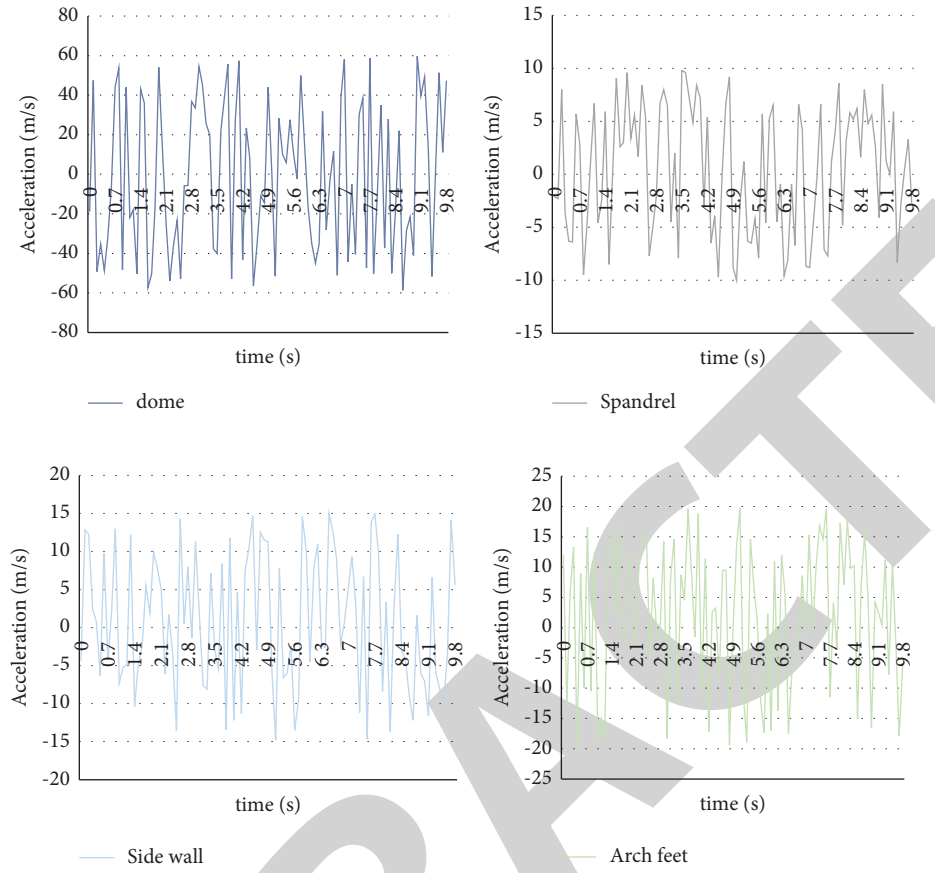

Figure 8: Acceleration time-history curve of each observation point of the conventional section of the upper-span tunnel.

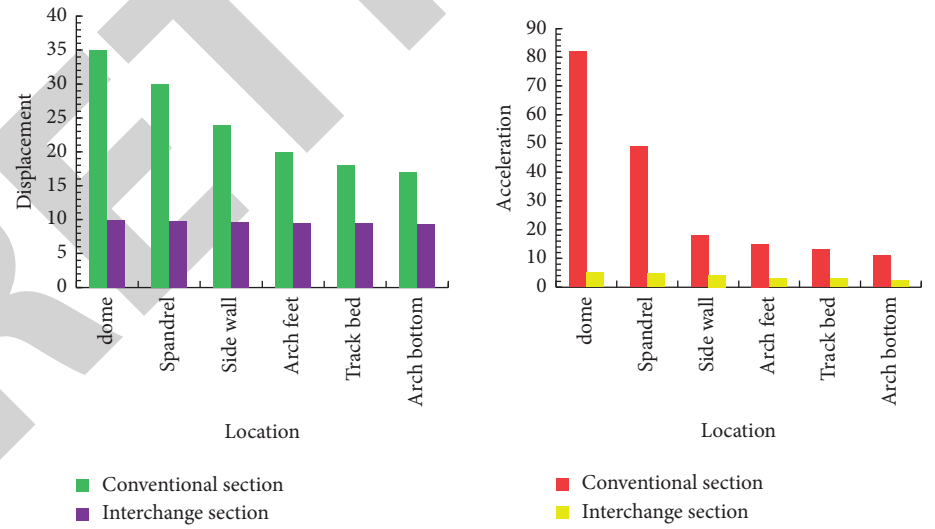

Figure 9: Vertical displacement changes and acceleration peak trends of each observation point.

of different content of nanomaterials on the wear resistance of steel.

During the wear test, there were only two stages running-in and stabilization. The average friction coefficient of the stable stage of steel without nano-CeO_2 was 0.58, and the average friction coefficient of the stable stage of steel with 0.004%, 0.012%, and 0.031% nano-CeO_2. They are 0.59, 0.47, and 0.45, respectively. After adding nano-CeO_2, the friction coefficient of steel at room temperature is lower than that of steel without nanoparticles.

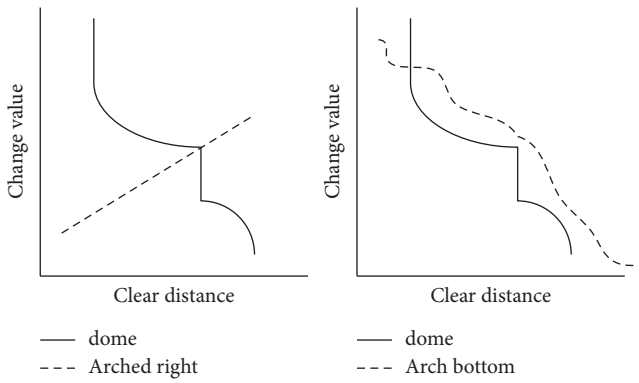

Figure 10: The trend diagram of the lining displacement value of the left-line tunnel.

The wear morphology of steel with different content of nano-CeO_2 has circular arc morphology, while the wear scar of steel without nano-CeO_2 is very wide and produces a lot of fatigue spalling. It is because of the relatively high hardness of the WC grinding ball for grinding, resulting in a softer steel matrix. During the wear process, the surface of the sample is constantly cut by friction, causing a large area of the wear scar surface to peel off. The main wear mechanism of steel with nano-CeO_2 is still fatigue spalling. When the amount of nano-CeO_2 added is small, the wear surface will peel off more, and the amount of wear will be greater; when the amount of nano-CeO_2 added reaches 0.012%, the wear surface will be smoother. There is almost no peeling, indicating that the sample has good friction and wear resistance. It is due to the addition of nano-CeO_2 that the steel structure has been refined, and the morphology and distribution of carbides have been significantly improved.

Through the previous analysis, it can be concluded that after adding different content of nano-CeO_2 particles, the core of the steel is coarser than the surface structure, and the solidified structure is improved. With the increase in the amount of addition, the length of the rod-shaped carbides gradually shortened, and a small amount of large agglomerated carbides began to appear, and then, the large block-shaped carbides tended to decompose into small carbides. When the CeO_2 content reaches 0.012%, the overall carbide morphology becomes more rounded. Compared with the sample without adding nano-CeO_2 particles, the impact performance of the steel after adding nano-CeO_2 particles is increased by 18.75%. When 0.012% CeO_2 is added, the impact toughness of the steel reaches the maximum value of 3.4 J, which is 16.31% higher than when it is not added. In addition, adding different content of nano-CeO_2 has little effect on the hardness of the steel.

The wear resistance of steel with nano-CeO_2 is better than that without CeO_2, and the overall wear resistance is improved by 37%. Experiments show that the larger the amount of nano-CeO_2, the better the wear resistance of steel. The wear is mainly manifested by fatigue spalling. The steel with 0.012% nano-CeO_2 has the lowest wear rate and the shallowest wear scar depth.

5. Conclusions

This article is based on the dynamic structure of the heavy-duty railway surrounding rock in the small clearance crossing tunnel. Considering that the heavy-duty railway damages the tunnel rock mass structure, the tunnel is prone to heavy load problems during actual use, the intermediate idle period is short, and the railway is not well maintained, which increases the use of the railway, and the loss of the railway is also increased exponentially. After the use of nanosprayed steel and ferroelectric domain polarization, the impact resistance of the steel is increased by 18.75%. When 0.012% of CeO_2 is added, the impact toughness of the steel is increased to the maximum of 3.4 J, which is an increase of 16.31%. The degree of wear resistance has been increased by 37% so that the strength of tunnels, railways, and arch waist structures can be greatly improved. Under the premise of maintaining the existing heavy-duty transportation strength, the consideration of transportation safety is also improved. Moreover, after the overall strength is increased, the later maintenance cost and maintenance neutral can also be reduced, which can greatly improve the efficiency of transportation.

Data Availability

The datasets used and/or analyzed during the current study are available from the corresponding author upon reasonable request.

Conflicts of Interest

The authors declare that they have no conflicts of interest.

References

[1] J. Rzayev, "Molecular bottlebrushes: new opportunities in nanomaterials fabrication," *ACS Macro Letters*, vol. 1, no. 9, pp. 1146–1149, 2012.

[2] M. Wiemann, A. Vennemann, U. G. Sauer, K. Wiench, L. Ma-Hock, and R. Landsiedel, "An in vitro alveolar macrophage assay for predicting the short-term inhalation toxicity of Nanomaterial's," *Journal of Nanobiotechnology*, vol. 14, no. 1, pp. 1–27, 2016.

[3] G. P. Lithoxoos, J. Samios, and Y. Carissan, "Investigation of silicon model nanotubes as potential candidate nanomaterials for efficient hydrogen storage: a combined ab initio/grand canonical Monte Carlo simulation study," *Journal of Physical Chemistry C*, vol. 112, no. 43, pp. 16725–16728, 2008.

[4] T. Yamaguchi, K. Asada, H. Yamakawa et al., "Photoexcitation of a one-dimensionalpolarization-inverted domain from the charge-ordered ferroelectric ground state of (TMTTF)_2PF_6," *Physical Review*, vol. 99, no. 24, Article ID 245104.1, 2019.

[5] H. W. Shin and J. Y. Son, "Ferroelectric domain structure and polarization switching speed of highly (111)-oriented polycrystalline YMnO3 thin films on glass substrates," *Thin Solid Films*, vol. 636, no. 31, pp. 247–250, 2017.

[6] A. M. Gonçalves, J. A. Eiras, F. A. Londono, and D. Garcia, "Domain structure and polarization reversal in ferroelectric lanthanum-modified lead titanate ceramics investigated by

piezoresponse force microscopy," *Journal of Materials Science*, vol. 51, no. 8, pp. 4061–4069, 2016.

[7] Q. S. Yan, M. Spiryagin, Q. Wu, C. Cole, and W. H. Ma, "Feasibility in assessing the dipped rail joint defects through dynamic response of heavy haul locomotive," *Journal of Modern Transportation*, vol. 26, no. 2, pp. 1–11, 2018.

[8] X. Cai, Y. Zhong, X. Hao, Y. Zhang, and R. Cui, "Dynamic behavior of a polyurethane foam solidified ballasted track in a heavy haul railway tunnel," *Advances in Structural Engineering*, vol. 22, no. 3, pp. 751–764, 2019.

[9] X. Xu, M. Fu, Z. Xu, and Z. Chen, "A new lever-type variable friction damper for freight bogies used in heavy haul railway," *Journal of Modern Transportation*, vol. 24, no. 3, pp. 159–165, 2016.

[10] K. Bhattacharya, S. P. Mukherjee, A. Gallud et al., "Biological interactions of carbon-based nanomaterials: from coronation to degradation," *Nanomedicine: Nanotechnology, Biology and Medicine*, vol. 12, no. 2, pp. 333–351, 2016.

[11] Y. Cai, L. Xu, W. Liu, Y. Shang, N. Su, and D. Feng, "Field Test Study on the dynamic response of the cement-improved expansive soil subgrade of a heavy-haul railway," *Soil Dynamics and Earthquake Engineering*, vol. 128, Article ID 105878, 2020.

[12] P. Liu, K. Wang, and D. Zhang, "Influence of traction and braking operation on wheel-rail dynamic interaction for heavy haul locomotive," *Zhongguo Tiedao Kexue/China Railway Science*, vol. 38, no. 2, pp. 96–104, 2017.

[13] D. E. Holder, M. V. Csenge, Y. Qian, M. S. Dersch, J. R. Edwards, and B. J. Van Dyk, "Laboratory investigation of the Skl-style fastening system's lateral load performance under heavy haul freight railroad loads," *Engineering Structures*, vol. 139, pp. 71–80, 2017.

[14] W. R. Liu, D. Y. Wang, K. Gao, and Z. Huang, "Design of distributed cooperative observer for heavy-haul train with unknown displacement," *IET Intelligent Transport Systems*, vol. 11, no. 4, pp. 239–247, 2017.

[15] J. B. Zhu, Y. S. Li, S. Y. Wu, R. Zhang, and L. Ren, "Decoupled explosion in an underground opening and dynamic responses of surrounding rock masses and structures and induced ground motions: a FEM-DEM numerical study," *Tunnelling and Underground Space Technology*, vol. 82, pp. 442–454, 2018.

[16] Y. Wang, H. Jing, H. Su, and J. Xie, "Effect of a fault fracture zone on the stability of tunnel-surrounding rock," *International Journal of Geomechanics*, vol. 17, no. 6, Article ID 04016135, 2017.

[17] B. I. Choi, D. H. Shin, D. H. Lee, and K. W. Kim, "Dynamic analysis of fill dam using 3D FEM analysis," *Japanese Geotechnical Society Special Publication*, vol. 2, no. 24, pp. 892–896, 2016.

[18] J. Lu, X. Meng, Y. Wang, and Z. Yang, "Prediction of coal seam details and mining safety using multicomponent seismic data: a case history from China," *Geophysics*, vol. 81, no. 5, pp. B149–B165, 2016.

[19] G. Wang and Y. Pang, "Surrounding rock control theory and longwall mining technology innovation," *International Journal of Coal Science and Technology*, vol. 4, no. 4, pp. 301–309, 2017.

[20] W. Yao, Y. Xu, W. Wang, and P. Kanopolous, "Dependence of dynamic tensile strength of longyou sandstone on heat-treatment temperature and loading rate," *Rock Mechanics and Rock Engineering*, vol. 49, no. 10, pp. 3899–3915, 2016.

[21] L. Huang, Z. Liu, C. Wu, and J. Liang, "The scattering of plane P, SV waves by twin lining tunnels with imperfect interfaces embedded in an elastic half-space," *Tunnelling and Underground Space Technology*, vol. 85, pp. 319–330, 2019.

[22] Y. Zengqiang, H. Zhu, L. Chang, F. Xie, L. Dou, and J. Chen, "Mechanism of rock burst caused by fracture of key strata during irregular working face mining and its prevention methods," *International Journal of Mining Science and Technology*, vol. 29, no. 6, pp. 78–86, 2019.

[23] X. Wang, J. Chen, and M. Xiao, "Seismic responses of an underground powerhouse structure subjected to oblique incidence SV and P waves," *Soil Dynamics and Earthquake Engineering*, vol. 119, pp. 130–143, 2019.

[24] Z. Yang, L. Dou, C. Liu, M. Xu, Z. Lei, and Y. Yao, "Application of high-pressure water jet technology and the theory of rock burst control in roadway," *International Journal of Mining Science and Technology*, vol. 26, no. 5, pp. 929–935, 2016.

[25] L. Yuan, M. Yang, and Z. Meng, "Soil pressure of the surrounding rock for a subway tunnel across ground fissures under a train load," *Modern Tunnelling Technology*, vol. 54, no. 4, pp. 63–67, 2017.